Electronic Supplementary Information (ESI)

Surface Hydroxyls and Oxygen Vacancies Dependent Cr(VI) Adsorption of BiOCl

*Guangming Zhan, Jie Li, Yue Hu, Shengxi Zhao, Shiyu Cao, Falong Jia, and Lizhi Zhang**

Key Laboratory of Pesticide & Chemical Biology of Ministry of Education, Institute of Environmental & Applied Chemistry, Central China Normal University, Wuhan 430079, P. R. China

19 pages, 5 text, 27 figures, 2 tables

* To whom correspondence should be addressed. E-mail: zhanglz@mail.ccnu.edu.cn(L. Zhang).
Phone/Fax: +86–27–6786 7535.

CONTENTS

Text S1. Characterizations. Powder X-ray diffraction (XRD) was recorded on a D8 Advance diffractometer with monochromatized Cu Kα radiation (λ = 0.15418 nm) (Bruker, German). The morphologies of the samples were observed using a scanning electron microscope (SEM, JEOL-6700F, Japan). Transmission electron microscopy (TEM) and high resolution TEM analysis were performed by using a transmission electron microscope (JSM-2010, JEOL, Japan) operating at a voltage of 200 kV. FTIR spectra of BiOCl were recorded by Nicolet iS50FT-IR spectrometer (Thermo, USA) after water desorption at 200 ^{o}C. The diffuse reflectance UV-visible spectra (DRS) of the samples were recorded on a UV-3600 spectrophotometer (Shimadzu, Japan) and $BaSO_4$ was used as a reflectance standard. XPS were collected using a Thermo Scientific K-Alpha XPS spectrometer with a monochromated X-ray source (Aluminum Kα) (Thermo, USA). The C 1*s* peak arising from adventitious hydrocarbons at the energy value 284.8 eV was used as an internal binding energy reference. Raman measurements were carried out by a confocal laser micro-Raman spectrometer (Thermo DXR Microscope, USA) with a 532 nm laser (5 mW). Low-temperature electron paramagnetic resonance (EPR) spectra were conducted on a Bruker EMX EPR Spectrometer (Billerica, MA).

Text S2. In situ ATR-FTIR spectroscopy. *In situ* ATR-FTIR analyses were performed by using a Nicolet iS50 FT-IR spectrometer (Thermo) equipped with a diamond internal reflection element (IRE). A liquid N_2-cooled mercury-cadmium-telluride (MCT) detector was used to record spectra in the range of 2000 to 600 cm^{-1} with consisted of 1024 averaged scans at a resolution of 4 cm^{-1}. 10 μL of 4 g/L BiOCl suspension was dropped on the diamond IRE and dried to form BiOCl films. The background spectrum was obtained after equilibrating the film with an electrolyte solution. After the film was reacted with Cr(VI) concentrations in a range of 5.0 to 100.0 mg/L and reached equilibrium, the final spectra were recorded.

Text S3. Cr K-edge XAFS spectroscopy. The XAFS spectra of Cr and Bi were performed at the beamline 1W1B of Beijing Synchrotron Radiation Facility, Institute of High Energy Physics, Chinese Academy of Sciences. The storage ring conducted at 2.2 GeV with currents about 100 mA. The scanning region of -50 eV to 50 eV around the absorption edge E_0 was about to XANES, and the region from 50 to 1000 eV above the edge E_0 was discernible as EXAFS. Incident X-ray energy was scanned across the XANES and EXAFS region of the Cr K-edge and Bi L-edge with using a Si (111) double crystal monochromator calibrated by Cr foil and Pt foil, respectively. After reaching the adsorption equilibrium of Cr(VI), we collected the BiOCl samples by high-speed centrifugation, washed with deionized water, and then dried in air. Obtained BiOCl samples were carefully and uniformly applied to 3M tape. The fluorescence mode was used for the samples of Cr(VI) adsorbed on BiOCl, and the transmission mode was used for reference compounds K_2CrO_4, Cr_2O_3 and Bi in BiOCl. The EXAFS data were converted to R-space by taking the Fourier transform of $\chi(k)$ function. Fitting was performed simultaneously on all data sets in R-space using the program Artemis to optimize the coordination number (CN), the distance (R), and disorder (σ^2). Phase and amplitude functions for the absorber and backscatterers were defined using the FEFF model. EXAFS wavelet transforms (WT) analysis was also applied to simultaneously decompose the EXAFS signal in the reciprocal and real spaces.

Text S4. Adsorption isotherms

The Cr(VI) adsorption equilibrium was studied by using Langmuir isotherm model and Freundlich isotherm model, respectively. The linear form of Langmuir equation is written as eq 1.

$$C_e/q_e = 1/(q_m K_L) + C_e/q_m \quad (1)$$

where C_e is the equilibrium concentration of Cr(VI) ions (mg/L), q_e is the amount of Cr(VI) adsorbed per unit surface area of the BiOCl nanosheets at equilibrium (mg/m^2), q_m (mg/m^2) is the maximum adsorption capacity, and K_L (L/mg) is the equilibrium constant.

The linear form of the Freundlich model could be represented as eq 2.

$$\ln q_e = \ln K_F + 1/n \ln C_e \quad (2)$$

where K_F ($(mg/m^2)(mg/L)^n$) and 1/n are Freundlich constants related to adsorption capacity and adsorption intensity, respectively.

Text S5. Quantitative relation between adsorbed Cr(VI) and surface defects of BiOCl.

As lattice constants of tetragonal BiOCl were a = b = 0.3883 nm, the maximum concentration of surface OHs:

$$\rho_{OH} = 2/a*b = 13.3 \text{ group/nm}^2$$

The conversion factor between OHs concentration and coverage:

$$\xi_{OH} = \rho_{OH}/100 = 13.3/100 = 0.133$$

Since OVs were produced from OHs thermal recombination (2*OH → OVs + *O + H_2O), the conversion factor between OVs concentration and coverage was half of ξ_{OH}.

$$\xi_{OV} = \xi_{OH}/2 = 0.0665$$

The conversion factor between Cr(VI) adsorption concentration (group/nm^2) and q_m (mg/m^2):

$$\xi_{Cr(VI)} = (10^{-3}*6.02*10^{23})/(51.996*10^9*10^9) = 11.6$$

The quantitative relation between adsorbed Cr(VI) and surface OHs and OVs of BiOCl was represented as eq 3 and eq 4, respectively.

$$\eta_{OH\text{-}Cr(VI)} = 1/k_{OH} * \xi_{OH}/\xi_{Cr(VI)} \quad (3)$$

$$=0.133/(2.94*10^{-3}*11.6) = 3.90$$

$$\eta_{OV\text{-}Cr(VI)} = 1/k_{OV} * \xi_{OV}/\xi_{Cr(VI)} \quad (4)$$

$$=0.0665/(4.31*10^{-3}*11.6) = 1.33$$

The k_{OH} and k_{OV} were the fitting slope of Cr(VI) adsorption capacity with the coverage degree of OHs and OVs on BiOCl as shown in Figure 3.

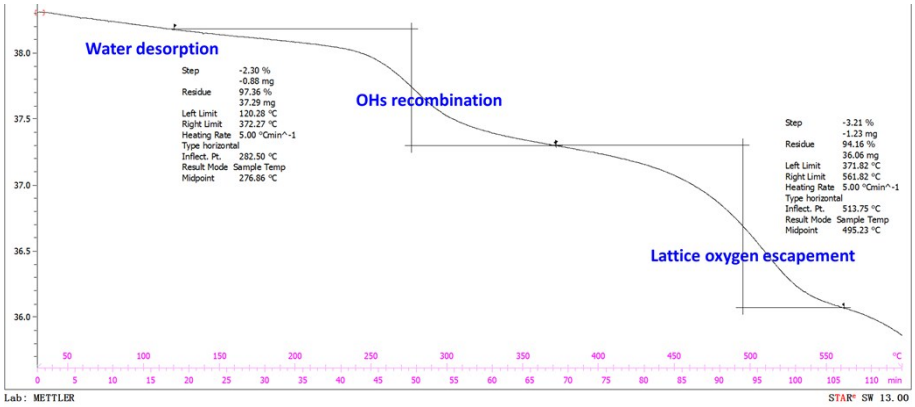

Figure S1. The thermogravimetric analysis curve of BiOCl-OH-1. Water was gradually desorbed from BiOCl-OH-1 as the temperature increased to 200 °C, and OHs thermal recombined before the temperature elevated to 350 °C. Moreover, the lattice oxygen of BiOCl escaped when the temperature was above 500 °C. To rule out its contribution to the generation of OVs, the BiOCl simples were calcined at 350 °C in this study.

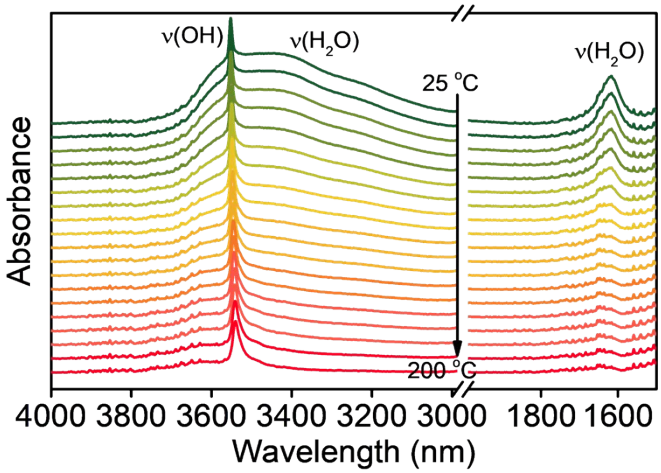

Figure S2. *In situ* FTIR of BiOCl-OH-1. Regarding that water could be adsorbed on BiOCl surface to interfere with the signal of OHs, we collected the *in situ* FTIR of BiOCl along with temperature increase. The signal of adsorbed water around 3400 cm^{-1} and 1620 cm^{-1} decreased with temperature increase and almost disappeared at 200 °C, which is in good agreement with the thermogravimetric analysis (SI Figure S1). Meanwhile, the sharp peak of OHs at 3550 cm^{-1} remained stable during the temperature increase from 25 °C to 200 °C. Therefore, we collected OHs FTIR signals of all BiOCl samples after water desorption at 200 °C in this study.

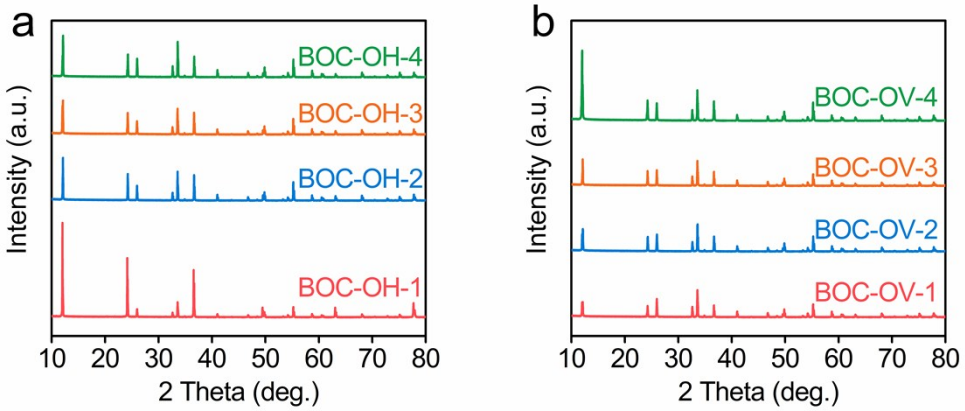

Figure S3. The XRD patterns of the prepared BOC-OH-X (a) and BOC-OV-X (X=1, 2, 3, and 4) (b).

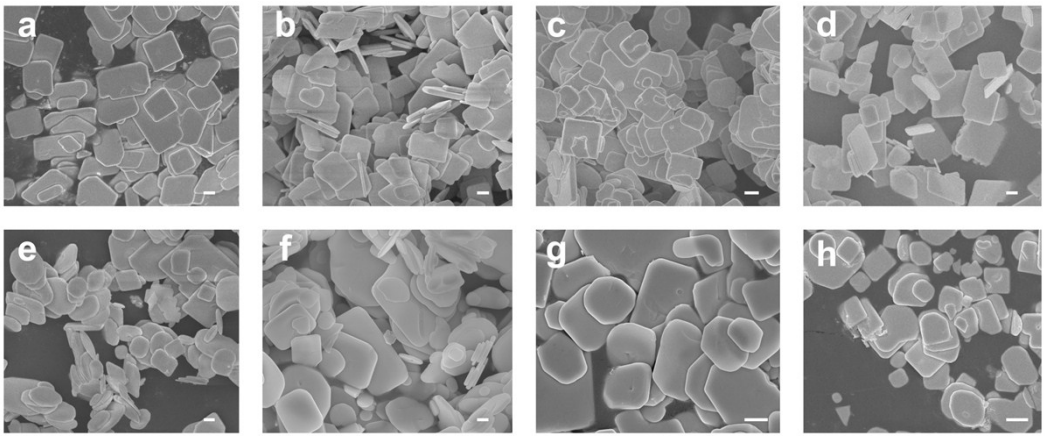

Figure S4. The SEM images of the prepared BOC-OH-X (a-d) and BOC-OV-X (X=1, 2, 3, and 4) (e-h). The scale bars are 500 nm.

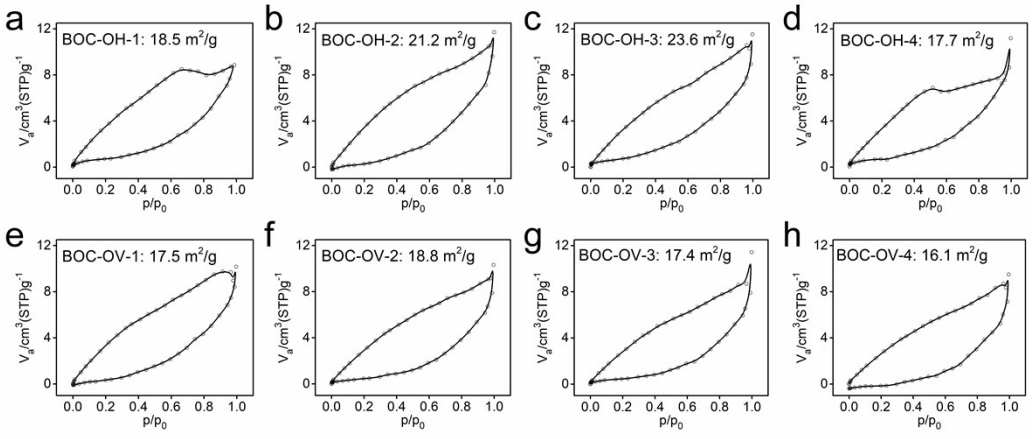

Figure S5. The specific surface area of the BOC-OH-X (a-d) and BOC-OV-X (X=1, 2, 3, and 4) (e-h).

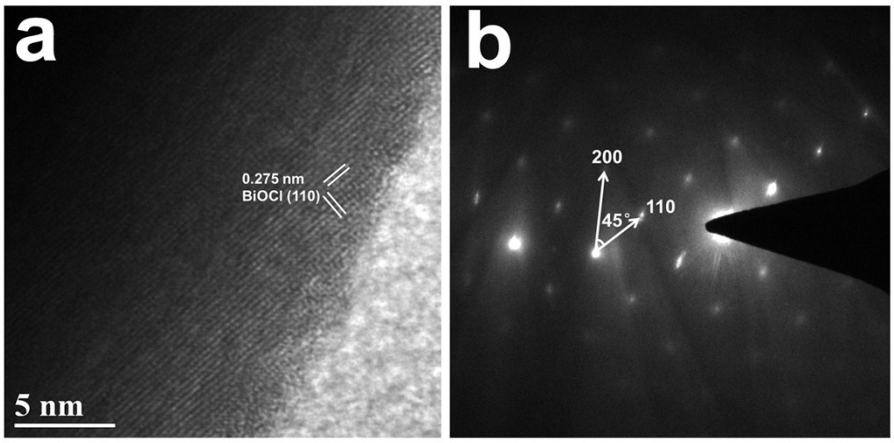

Figure S6. The HRTEM images and the corresponding selected-area electron diffraction (SAED) pattern of the prepared BiOCl-OH-1.

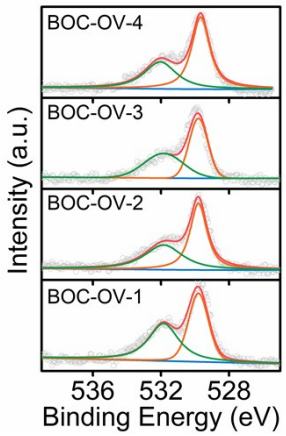

Figure S7. The high-resolution O 1s XPS spectra of prepared BOC-OV-X (X=1, 2, 3, and 4).

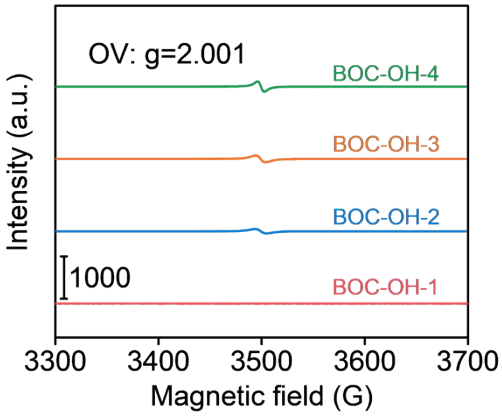

Figure S8. EPR spectra of BOC-OH-X (X = 1, 2, 3, and 4).

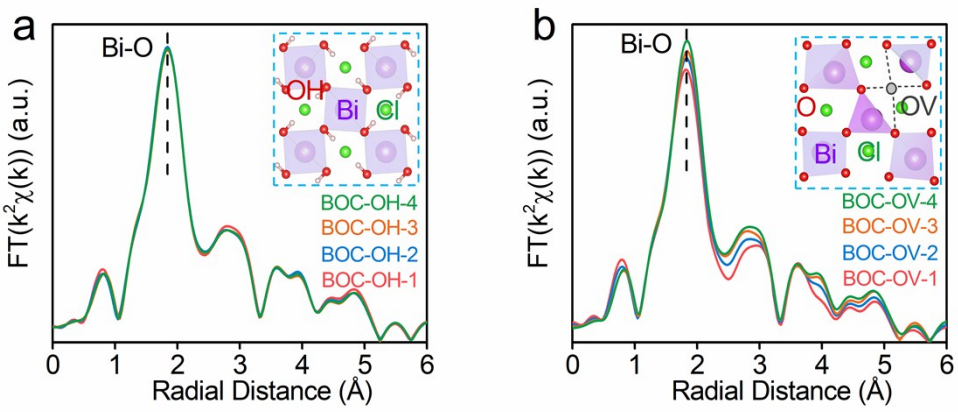

Figure S9. Bi L-edge EXAFS of prepared BOC-OH-X and BOC-OV-X (X=1, 2, 3, and 4), respectively. The inserts corresponding the top-view of BOC-OH and BOC-OV structure, respectively.

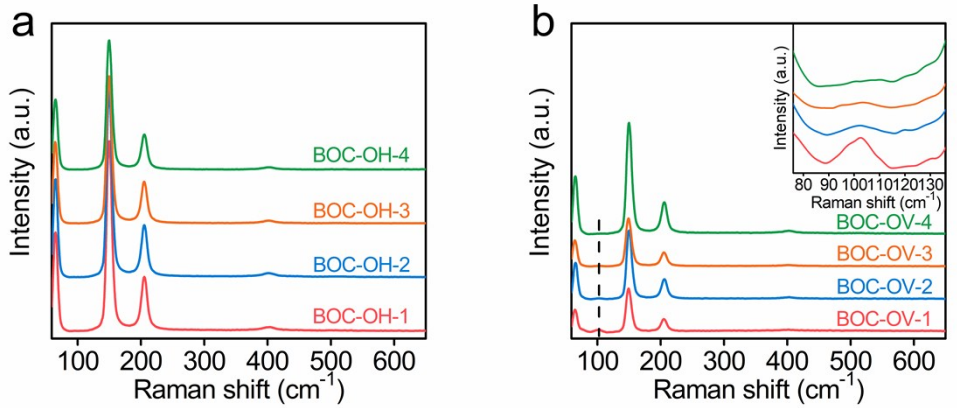

Figure S10. The Raman spectra of the prepared BOC-OH-X (a) and BOC-OV-X (X=1, 2, 3, and 4) (b).

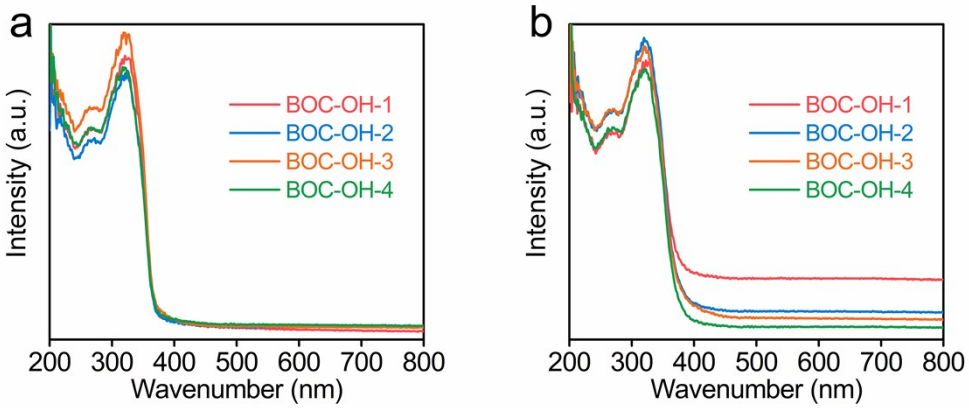

Figure S11. The UV-vis diffuse reflection spectroscopy of the prepared BOC-OH-X (a) and BOC-OV-X (X=1, 2, 3, and 4) (b).

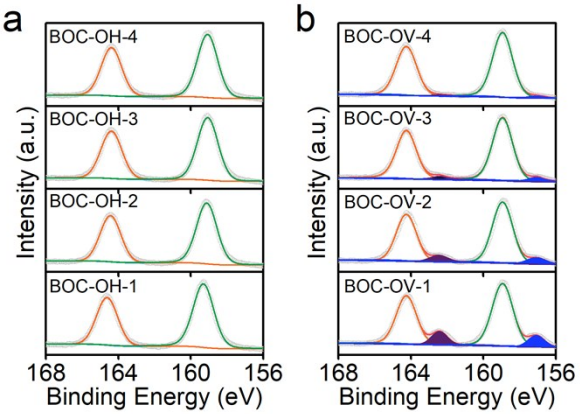

Figure S12. The high-resolution Bi 4f XPS spectra of the prepared BOC-OH-X (a) and BOC-OV-X (X=1, 2, 3, and 4) (b).

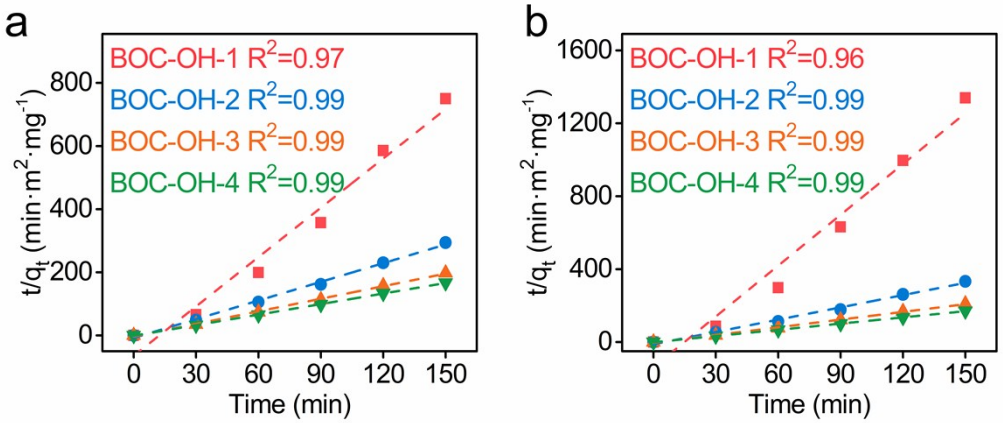

Figure S13. The corresponding pseudo-second-order removal kinetics curves of Cr(VI) ions on BOC-OH (a) and BOC-OV (b) under pH 9.

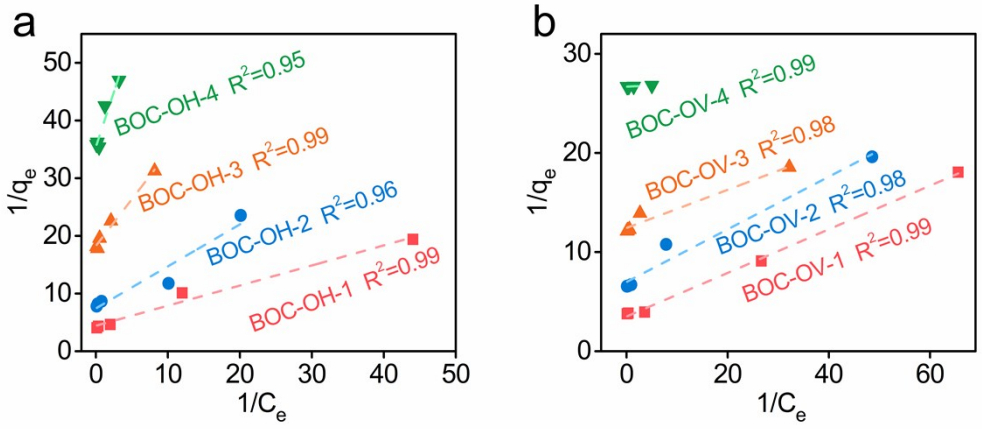

Figure S14. Langmuir plot for the adsorption of Cr(VI) by BOC-OH (a) and BOC-OV (b). The concentration of BiOCl was 0.5 g/L. The initial Cr(VI) ions concentrations ranged from 0.5 to 10.0 mg/L.

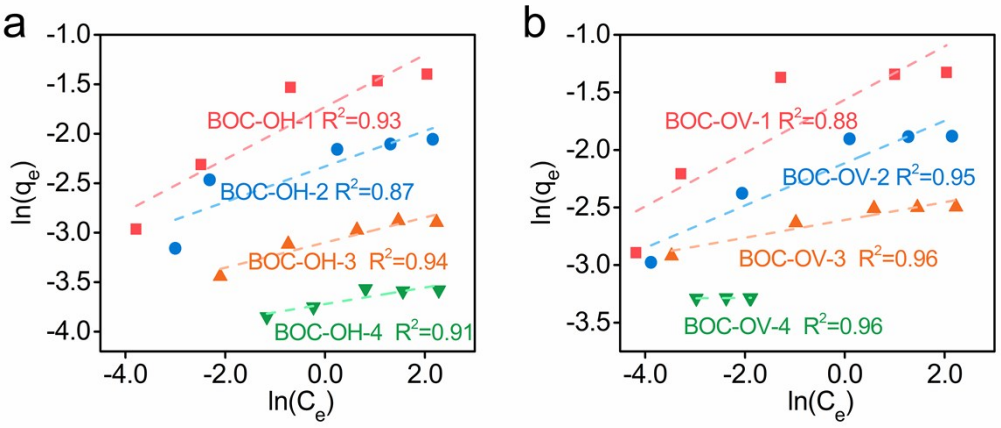

Figure S15. Freundlich plot for the adsorption of Cr(VI) by BOC-OH-X (a) and BOC-OV-X (X=1, 2, 3, and 4) (b). The concentration of BiOCl was 0.5 g/L. The initial Cr(VI) ions concentrations ranged from 0.5 to 10.0 mg/L.

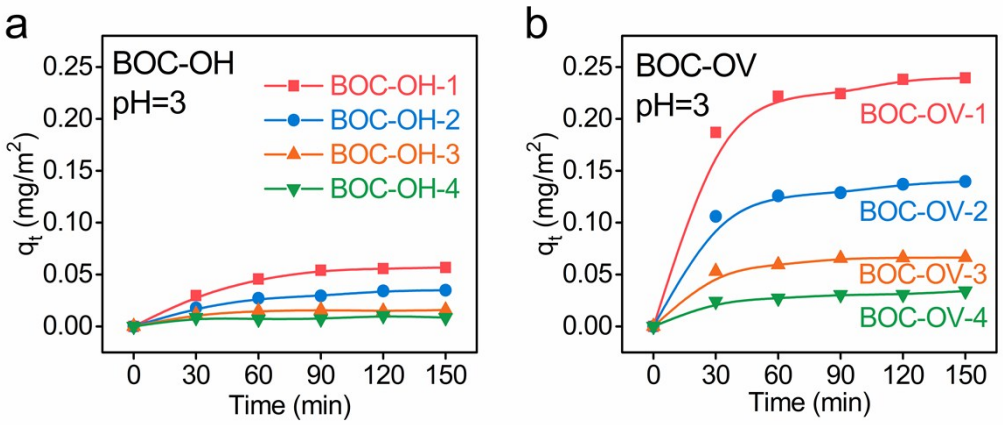

Figure S16. Time profile of Cr(VI) removal with a serious of surface defects covered BOC-OH (a) and BOC-OV (b) under acidic condition.

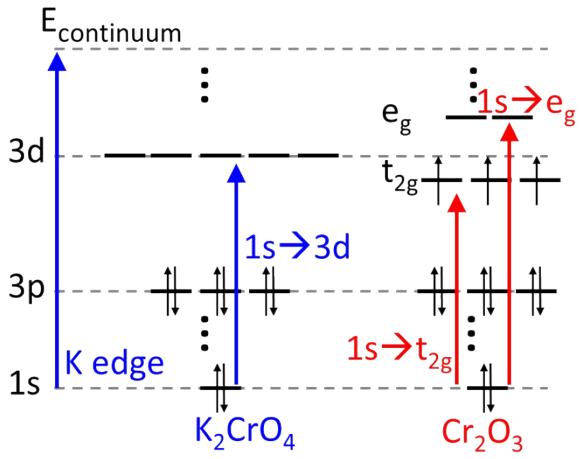

Figure S17. The electronic transition mechanism of Cr at K_2CrO_4 and Cr_2O_3 in XANES spectra.

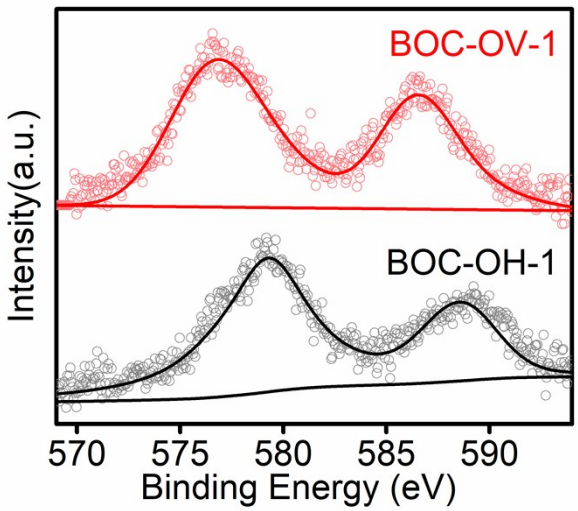

Figure S18. The high-resolution Cr 2p XPS spectra adsorbed on BOC-OH-1 and BOC-OV-1.

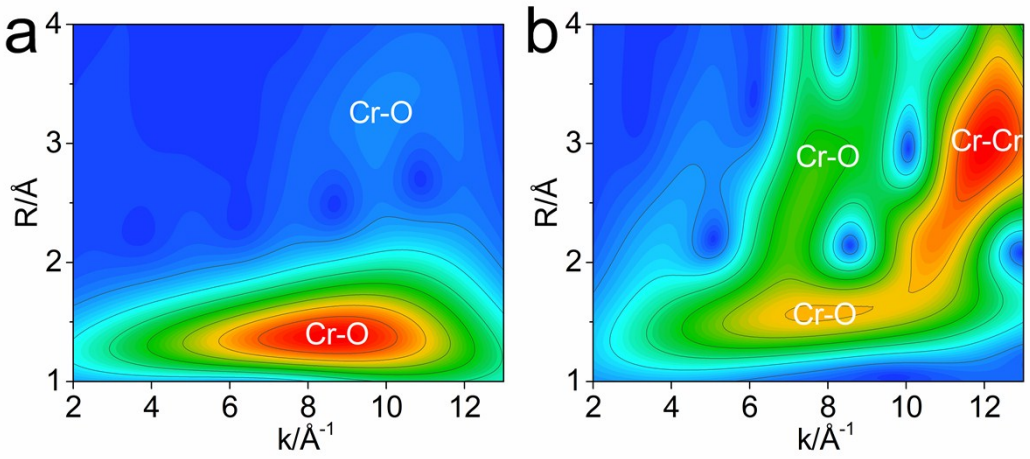

Figure S19. Wavelet transforms for the k^3-weighted EXAFS signals of Cr in standard simples of K_2CrO_4 (a) and Cr_2O_3 (b).

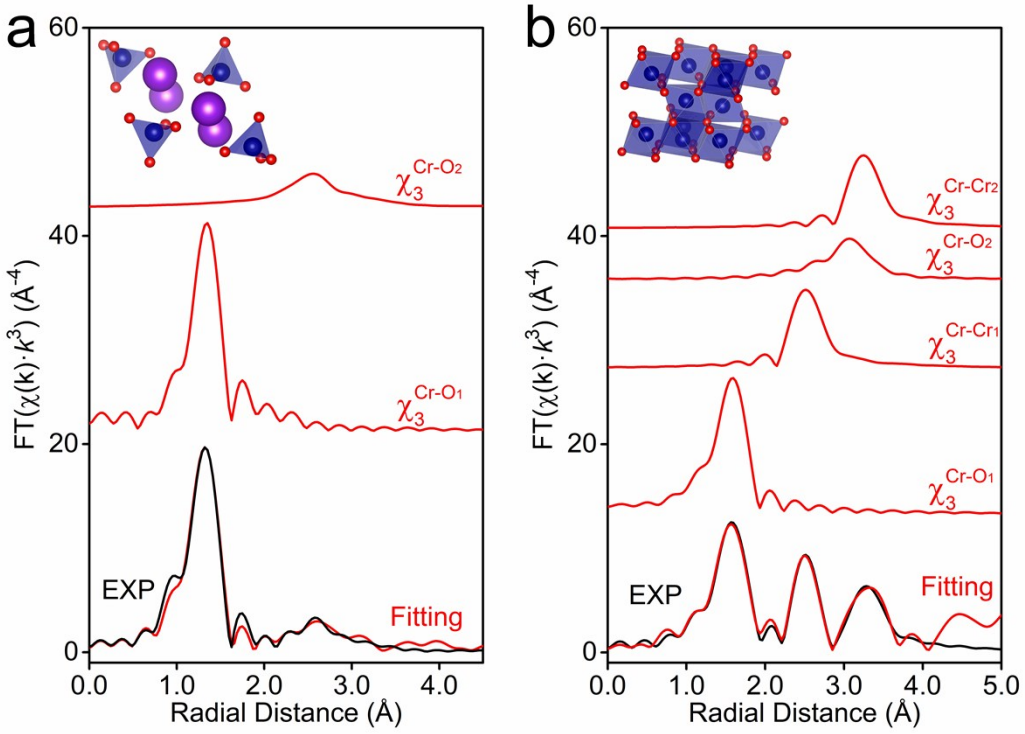

Figure S20. Cr k^3-weighted K-edge EXAFS of standard simples of K_2CrO_4 (a) and Cr_2O_3 (b), where the total fitting signal (red line) is superimposed on the experimental signal (black line). The Fourier transforms are not corrected for phase shift. The inserts in (a, b) are crystal structures of K_2CrO_4 and Cr_2O_3, respectively.

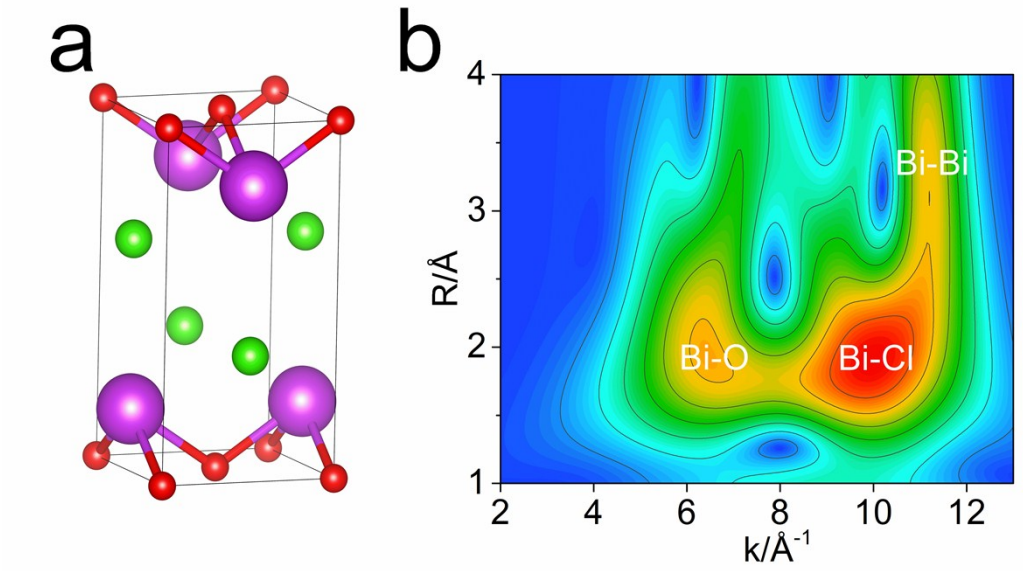

Figure S21. Crystal structures of BiOCl (a) and wavelet transforms for the k^3-weighted EXAFS signals of Bi in BiOCl.

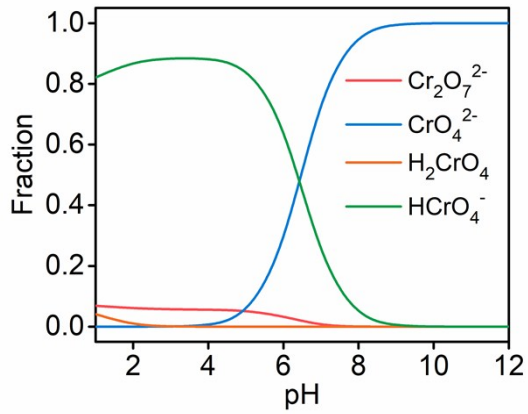

Figure S22. Cr(VI) speciation as a function of pH (reference Cr(VI) concentration 100 ppm.

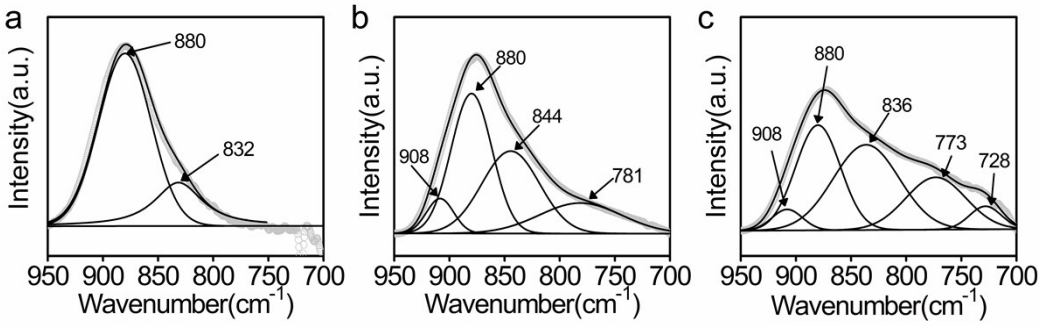

Figure S23. The peak positions used to fit the spectrum of CrO_4^{2-} adsorbed on BiOCl were held constant for the fitting of the spectrum.

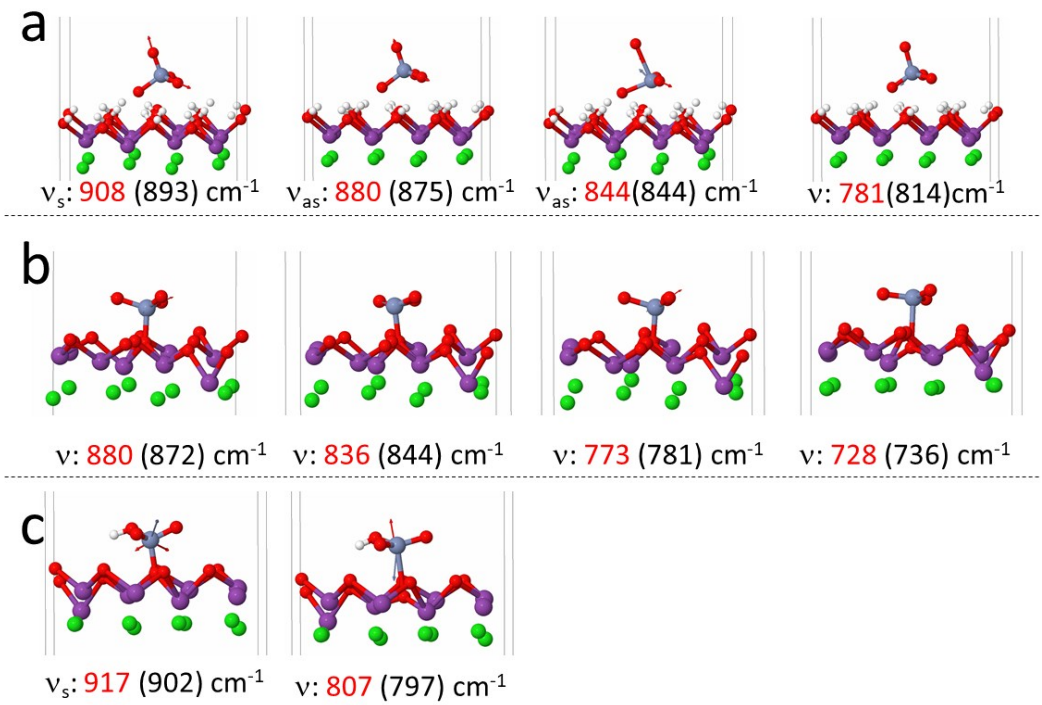

Figure S24. Specific IR vibration mode of i*n situ* ATR-FTIR spectroscopy (Red) and DFT frequency simulation (black, bracket) for CrO_4^{2-} adsorbed on BOC-OH (a), CrO_4^{2-} adsorbed on BOC-OV (b) and $HCrO_4^-$ adsorbed on BOC-OV.

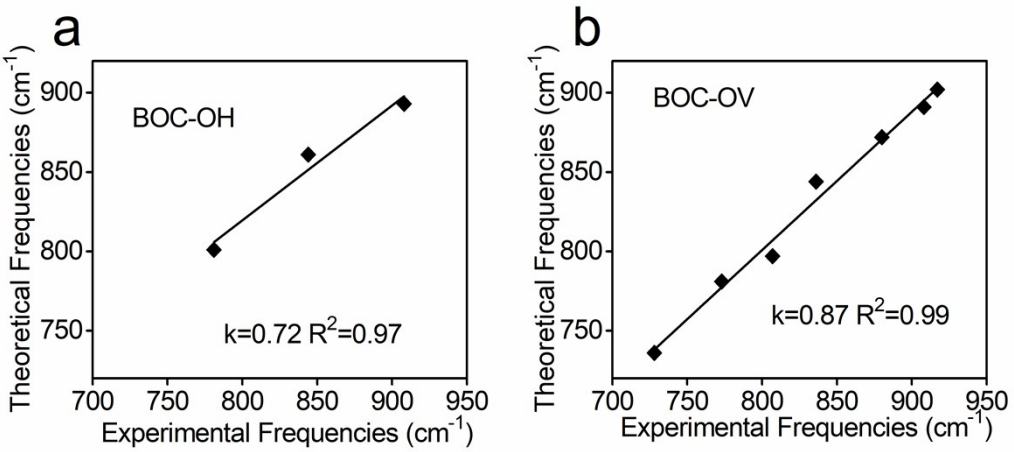

Figure S25. Correlation between theoretical and experimental frequencies of adsorbed CrO_4^{2-} (a) and $HCrO_4^-$ (b).

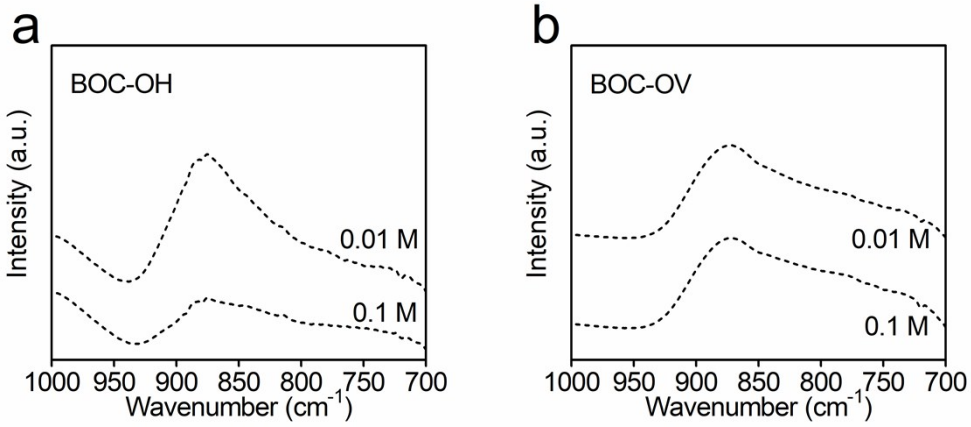

Figure S26. Effect of ionic strength on Cr(VI) adsorption. (a) ATR-FTIR spectra of Cr(VI) adsorption on BOC-OH-1 (a) and BOC-OV-1 (b) at pH 10 as a function of NaCl solution. The NaCl concentration were 0.01 and 0.10 mol/L, respectively

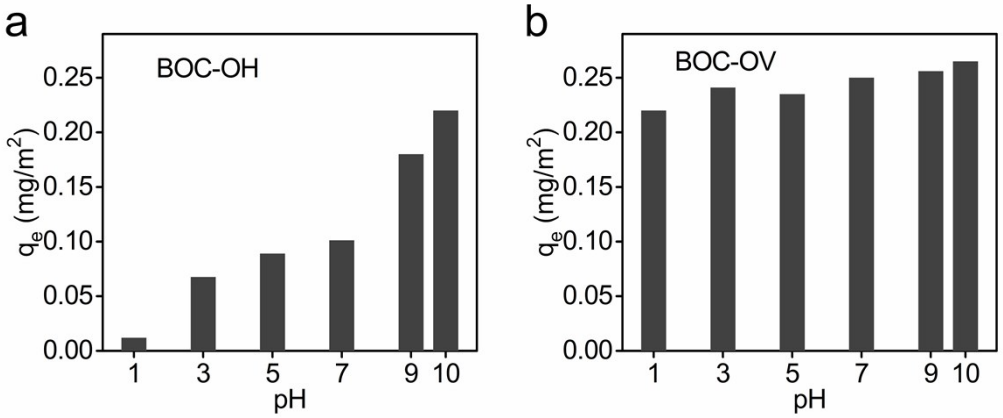

Figure S27. The Cr(VI) adsorption capacity of BOC-OH-1 (a) and BOC-OV-1 (b) at different initial pH values.

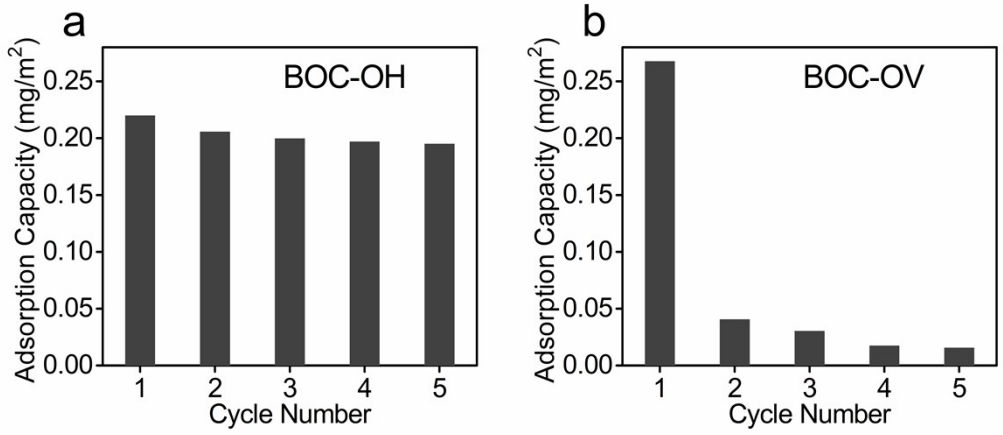

Figure S28. The adsorption capacity of BOC-OH (a) and BOC-OV (b).

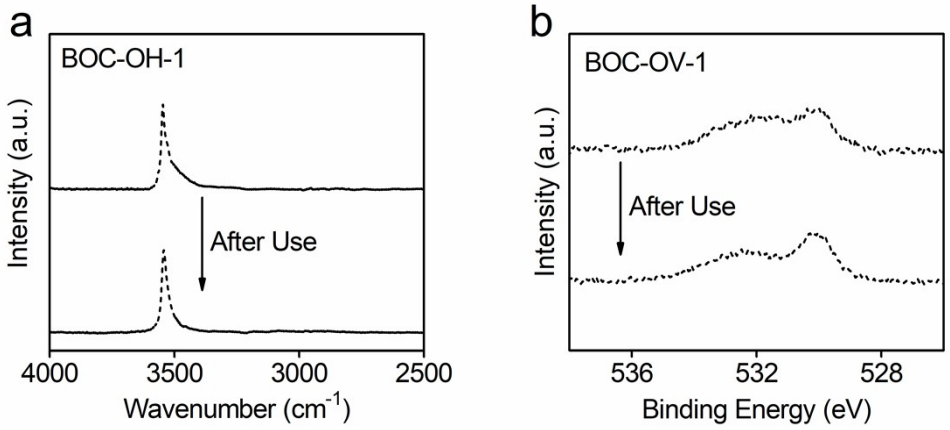

Figure S29. The FTIR and high-resolution O 1s XPS spectra of BOC-OH-1 before and after saturated adsorption of Cr(VI).

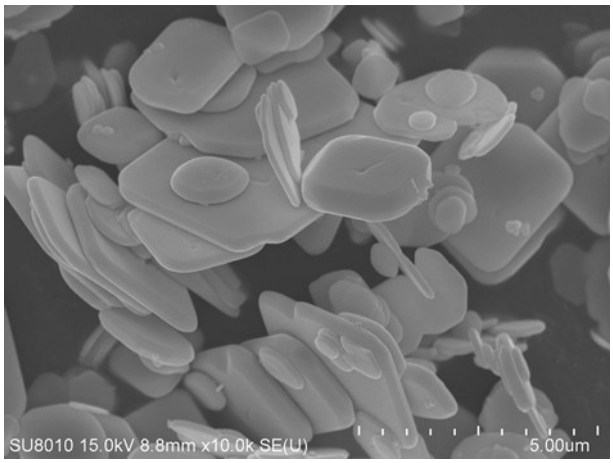

Figure S30. The SEM image of used BOC-OV-1.

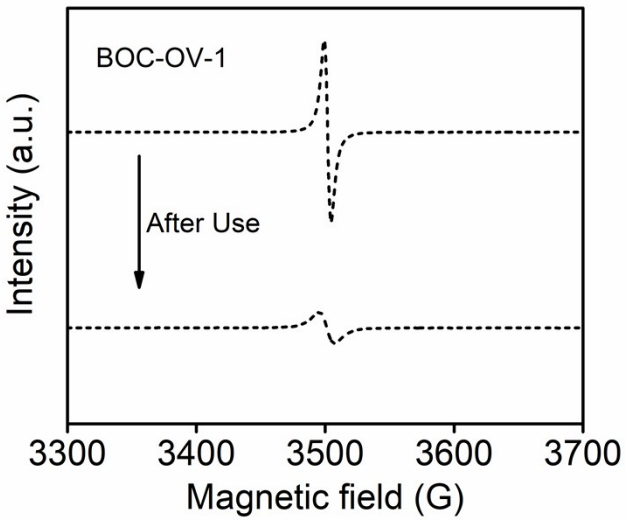

Figure S31. The EPR spectra of BOC-OV-1 before and after saturated adsorption of Cr(VI).

Table S1. DFT simulation results of Cr(VI) adsorbed on BiOCl nanosheets.

Samples	Adsorption Energy/eV	Electron transfer/e	HB Length/Å	Cr-O Length/ Å
$HCrO_4^-$ on BOC-OH	-0.29	0.02	1.83 1.84 2.33	1.86 (Cr-OH) 1.69 1.66 1.66
$HCrO_4^-$ on BOC-OV	-1.71	0.46	2.08	1.79 (Cr-OH) 1.78 (Cr-O-Bi) 1.60 1.60

Table S2. The maximum Cr(VI) adsorption capacity comparison of BiOCl, natural material based adsorbents and recently reported adsorbents. (SSA: specific surface area)

Samples	SSA(m^2/g)	q_m(mg/g)	q_m(mg/m^2)	Reference
BOC-OH-1	18.5	4.07	0.22	This work
BOV-OV-1	17.5	5.08	0.29	
Goethite-acidic	79	11.30	0.143	*Environ. Sci.: Nano* 2019, **6**, 2185.
Goethite-alkaline	46	4.65	0.101	
flowerlike α–Fe_2O_3	120	30	0.23	*Langmuir* 2012, **28**, 4573.
flowerlike α–Fe_2O_3	40	5.4	0.14	*Adv. Mater.* 2006, **18**, 2426.
HNPs	20.9	7.94	0.38	*Environ. Sci. Technol.* 2016, **50**, 1964.
HNRs	2.6	1.66	0.64	

Table S3. The fitting parameters of Cr K-edge Fourier-filtered k^3-weighted EXAFS for standard simples, Cr(VI) adsorbed on BOC-OH-1 and BOC-OV-1 nanosheets. [a] R is the absorber-backscatterer distance. [b] CN is the number of backscattering atoms around the absorbing Cr atom. [c] σ^2 is the Debye-Waller value.

Samples	Path	R (Å)[(a)]	CN[(b)]	σ^2 (10^{-3}Å^2)[(c)]	E_0 (eV)	R_f (%)
K_2CrO_4	Cr-O	1.63±0.01	3.2±0.2	2.3±0.3	15.1±0.8	1.51
	Cr-O	3.02±0.03	8.4±0.6	3.9±0.6	9.7±0.6	
Cr_2O_3	Cr-O	1.99±0.02	4.8±0.3	3.8±0.4	2.6±0.4	1.63
	Cr-Cr	2.89±0.01	1.8±0.4	1.2±0.1	2.7±0.7	
	Cr-O	3.64±0.03	4.2±0.5	1.9±0.4	1.7±0.8	
	Cr-Cr	3.92±0.04	3.9±0.6	2.7±0.5	5.3±0.6	
Cr(VI) on BOC-OH	Cr-O	1.63±0.04	3.1±0.4	1.1±0.1	10.2±0.1	1.91
Cr(VI) on BOC-OV	Cr-O	1.68±0.02	3.4±0.2	5.9±0.2	11.7±0.4	1.18
	Cr-O	3.08±0.04	2.7±0.5	4.9±0.7	9.5±0.6	
	Cr-Bi	3.61±0.05	0.9±0.4	7.1±0.2	2.3±0.7	